Volume 1 | Number 1 | Jan 2013 | Pages 1–100

Journal of
Materials Chemistry C

Materials for optical and electronic devices
www.rsc.org/materialsC

ROYAL SOCIETY
OF CHEMISTRY

ROYAL SOCIETY
OF CHEMISTRY

www.rsc.org/materialsC

First-principles study of the spin transport properties of 4H-TAHDI-based multifunctional spintronic device with graphene nanoribbon electrodes

P. Zhao[a,*], Q.H. Wu[a], H.Y. Liu,[a] D.S. Liu[b,c] G. Chen[a,*]

[a]*School of Physics and Technology, University of Jinan, Jinan 250022, China*

[b]*School of Physics, State Key Laboratory of Crystal Materials, Shandong University, Jinan 250100, China*

[c]*Department of Physics, Jining University, Jining 273155, China*

ABSTRACT

By using the nonequilibrium Green's function formalism in combination with the density functional theory, we have investigated the spin transport properties of 4H-TAHDI-based multifunctional spintronic device constructed by 4H-TAHDI molecule contacted with two ferromagnetic zigzag-edge graphene nanoribbon electrodes. The results show that perfect giant magnetoresistance, spin-filtering, bipolar spin-rectifying, and negative differential resistance effects can be realized simultaneously. The mechanisms were proposed for these interesting phenomena. Our results demonstrate that this system holds promise in the design of a high-performance multifunctional single-molecule spintronic device.

―――――

[*]School of Physics and Technology, University of Jinan, Jinan 250022, China. *E-mail:* ss_zhaop@ujn.edu.cn (P. Zhao) and ss_cheng@ujn.edu.cn (G. Chen).

1　Introduction

Spintronics is a novel discipline that seeks to exploit the intrinsic spin degree of freedom of an electron in addition to its charge. By introducing the spin degree of freedom, one can store more data with less physical space.[1] Up to now, most of the spintronic devices are based on inorganic materials. Many interesting phenomena, such as giant magnetoresistance (GMR),[2] spin-filtering,[3,4] Kondo effect,[5] and spin crossover[6,7] have been observed in these spintronic devices. In fact, organic molecules are more desirable for spintronics because they typically have small spin-orbit and hyperfine interactions, which are prerequisites for spintronic applications, due to allowing long spin coherence length.[8-10] Thus, much effort has been devoted to find the potential organic molecules to realize high-performance spintronic devices. For example, Schmaus *et al.*[11] observed magnetoresistance up to 60% in a hydrogen-phthalocyanine molecule coupled to two cobalt electrodes. Shen *et al.*[12] found that manganese-phthalocyanine and iron-phthalocyanine molecules contacted with single-walled carbon nanotube electrodes can function as good spin filters. Xu *et al.*[13] obtained spin-filtering behavior in a C_{28} fullerene sandwiched between two gold electrodes. Cho *et al.*[14] demonstrated that one-dimensional (1D) chromium-porphyrin array linked to gold electrodes can act as spin filter. Currently, there is a great interest in designing multifunctional spintronic devices (devices can show three or more functions meanwhile), since they are very important for the improvement of the integration density of atomic-scale circuits in future. Very recently, Zeng and Chen[15] investigated the spin transport properties of manganese-porphyrin-based spintronic devices, and found spin-filtering, magnetoresistance, and negative differential resistance (NDR) effects.

Graphene nanoribbons (GNRs), the 1D strips of graphene, are considered as promising

candidates for quantum electronic devices owing to their atomistic size,[16,17] unique electronic structures,[18,19] and outstanding transport properties.[18,20,21] There are two primary categories of GNRs: armchair- and zigzag-edge GNRs (AGNRs and ZGNRs).[22,23] Among them, ZGNRs hold the promise of spintronics due to their peculiar edge states and edge magnetism.[24] The ground state of ZGNRs is antiferromagnetic (AF) state with zero total magnetic moment:[25] the atoms on the lower (upper) edge are up- (down-) spin polarized. This severely limits its application for spintronics. However, it has been demonstrated that ZGNRs can be magnetized to the ferromagnetic (FM) state by applying a suitable transverse electrical field[26] or a magnetic field[27] and then can be used as electrodes in spintronics for spin injection.[28]

Hydroazaacene derivative have recently drawn great attention due to their potential application as organic semiconductive materials. 4H-TAHDI (terahydroteraazahexaacene diimide) molecule, a derivative of hydroazaacene with completely planar polycyclic framework, displays appealing optical properties and self-assembling behaviors.[29-31] In the present work, we designed a 4H-TAHDI-based multifunctional spintronic device with two FM ZGNR electrodes. The results show that the device can present perfect GMR, spin-filtering, bipolar spin-rectifying, and NDR effects simultaneously.

2   Model and computational details

Fig. 1(a) shows the designed molecular device, which can be partitioned into three regions: the left electrode (LE), the central scattering region (CSR), and the right electrode (RE). We chose 4-ZGNR as the electrodes, where the number 4 is the number of zigzag carbon chain (ZCC) along the direction perpendicular to the nanoribbon axis,[22] since it has been demonstrated that bipolar

spin-rectifying can only be realized in ZGNR with an even number of ZCC.[32] The dangling bond

of each edge carbon atom is terminated by a hydrogen atom. The CSR includes the 4H-TAHDI

molecule and portions of two ZGNR electrodes to take into account the molecule-electrode

coupling and the electrode screening effect. We have chosen a supercell with a large enough

vacuum layer in the directions perpendicular to the transport direction so that the device has no

interaction with its mirror images. As the magnetic fields at two electrodes can point in the same

or opposite direction, the magnetization of the device can be set to parallel (P) or antiparallel (AP)

spin configuration.

Our first-principles spin transport calculations were performed by the Atomistix Toolkit (ATK)

package,[33-36] which adopts the spin-polarized density functional theory (DFT) in conjunction with

the nonequilibrium Green's function (NEGF) formalism. In all calculations, the generalized

gradient approximation (GGA) with a Perdew-Burke-Ernzerhof (PBE) functional[37] was utilized to

calculate the electron exchange-correlation. Each atomic core for all atoms was described by

norm-conserving Troullier-Martins pseudopotentials,[38] and the valence electrons' wave function

was expanded in a single-ζ plus polarization (SZP) basis set since it is good enough in our

cases.[39,40] The cutoff energy was set to 150 Ry. The Brillouin zone samplings were done using

$1\times1\times100$ Monkhorst-Pack grids.[41] The atoms of CSR were fully relaxed until the force acted on

each atom is less than 0.02 eV/ Å. The spin-polarized current through the device is calculated

using the Landauer-Büttiker formula[42]

$$I_{\sigma}(V) = (e/h)\int_{\mu_L}^{\mu_R} T_{\sigma}(E,V)[f_L(E-\mu_L) - f_R(E-\mu_R)]dE, \tag{1}$$

where $f_{L(R)}$ and $\mu_{L(R)}$ are the Fermi-Dirac distribution function and the electrochemical

potential of the LE (RE), respectively. $T_{\sigma}(E,V)$ is the spin-resolved transmission function for

the spin-up (σ = up) and spin-down (σ = dw) electrons incident at an energy E through the device under the applied bias V, defined as

$$T_\sigma(E,V) = Tr[\Gamma_L G_\sigma^R \Gamma_R G_\sigma^A], \qquad (2)$$

where $G_\sigma^{R(A)}$ is the spin-dependent retarded (advanced) Green function of the CSR, $\Gamma_{L(R)}$ is the coupling matrix between the CSR and the LE (RE). Thus, the current is determined by the integral of $T_\sigma(E,V)$ over the energy region, [μ_L , μ_R], which is referred to as the bias window.

3   Results and discussions

We first calculated the magnetic moment (MM) of the free 4H-TAHDI molecule, and found the molecular MM is 0 μ_B . Then, as shown in Fig. 1(b), we presented the spin density distribution across the CSR region for P and AP spin configurations. The red and cyan colors stand for the up- and down-spin components, respectively. It is evident that the magnetism mainly distributes on the edged carbon atoms of ZGNR electrodes, and there is still no spin density distribution on the central 4H-TAHDI molecule. Fig. 2(a) displays the calculated total current-voltage (*I-V*) curves for P and AP spin configurations. Fig. 2(b) and (c) present the spin-resolved *I-V* curves for two spin configurations, respectively. Several interesting features can be found from these *I-V* curves: (1) as shown in Fig. 2(a), the total current of P spin configuration is much bigger than that of the AP spin configuration at low bias, which leads to a high GMR effect. The magnetoresistance ratio (MR) of GMR can be calculated using the equation

$$MR = [(I_P - I_{AP})/I_{AP}] \times 100\%, \qquad (3)$$

where I_P and I_{AP} are the total current in the P and AP spin configurations, respectively. As shown in Fig. 3(a), giant MR is obtain at the bias range from -0.3 to 0.3 V, especially, the MR almost

keeps unchanged as high as 2.6×10^6% at a bias up to $\pm$ 0.1 V, which is much bigger than those

reported previously.[43,44] (2) For the P spin configuration in Fig. 2(b), both the up-spin (I_{P_up}) and

down-spin current (I_{P_dw}) show highly symmetric behaviors due to the intrinsic structure and spin

symmetries. The I_{P_up} displays linear characteristics and increases rapidly before $\pm$ 0.7 V, while the

I_{P_dw} is blocked in the whole bias range. This indicates that the device shows perfect spin-filtering

effect in the P spin configuration. For the AP spin configuration in Fig. 2(c), both the up-spin

(I_{AP_up}) and down-spin current (I_{AP_dw}) show highly asymmetric behaviors due to the spin

asymmetry. The I_{AP_dw} (I_{AP_up}) can easily penetrate the device when the positive (negative) bias

exceeds 0.2 (-0.2) V, while it is almost forbidden within the bias range from -1.25 (-0.2) to 0.2

(1.25) V. Namely, the device in the AP spin configuration presents bipolar spin-filtering effect: the

down-spin channel is conducting (> 0.2 V) and the up-spin channel is insulating at positive bias,

while the case is complete opposite at negative bias. The observed spin-filtering effect can be

quantified by the bias-dependent spin-filtering efficiency (SFE):

$$SFE = (I_{up} - I_{dw})/(I_{up} + I_{dw}), \tag{4}$$

where I_{up} and I_{dw} are the up- and down-spin current for two spin configurations, respectively.

The SFE as a function of applied bias for two spin configurations is shown in Fig. 3(b). Clearly,

for the P spin configuration, the SFE reaches nearly 100% in the whole bias range. For the AP spin

configuration, the SFE is very small in low bias range from -0.1 to 0.1 V, and then it also reaches

nearly $\mp$ 100% in the remaining positive and negative bias range, respectively. This shows that

our device can displays perfect spin-filtering behavior in two spin configurations in such a wide

bias range, which is very desirable for practical applications. (3) It is evident that the device in the

AP spin configuration also reveals bipolar spin-rectifying effect. To further quantify the rectifying

performance, we define the bias-dependent rectification ratio (RR) as follows:

$$RR = \left| I_{neg} / I_{pos} \right| \text{ (for up-spin) or } \left| I_{pos} / I_{neg} \right| \text{ (for down-spin)}, \qquad (5)$$

where I_{pos} and I_{neg} are the spin-polarized current at positive and negative bias, respectively. As

shown in Fig. 3(c), the order of magnitude of RR varies from 10^2 to 10^4 in the bias range of [-1.25,

-0.1 V] and [0.1, 1.25 V], and the maximum RR can be up to 4.40×10^4 at -0.4 V and 5.02×10^4 at

0.55 V for up- and down-spin electrons, respectively, which are larger than that in previously

study.[45,46] The observed asymmetry of rectification ratio curve in Fig. 3(c) may be due to the small

asymmetry in the optimized structure. (4) Obvious NDR effect can be observed in the I_{P_up} and

I_{AP_up}/I_{AP_dw}. The NDR effect, which is characterized by an increasing followed by a deceasing

current with increasing bias in some specific bias range, has gained applications in a wide range

including memory,[47] switching,[48] amplification,[49] and logic circuits,[50] and so on. As shown in Fig.

2(b) and (c), the I_{P_up} and I_{AP_up}/I_{AP_dw} exhibit the NDR behaviors at $\pm$ 0.7 and $\mp$ 0.65 V, with a

peak-valley ratio (PVR) of ~10 and 12, respectively. Here, the PVR is defined as the ratio of the

peak current to the valley current.

To elucidate these interesting effects, in Fig. 4, we plotted the spin-resolved transmission as a

function of both electron energy and bias for two spin configurations. The zero-bias transmission

spectrum has been marked in red for clarity. The region between two dashed blue lines indicates

the bias window. Fig. 4(a) and (b) correspond to the up- and down-spin transmission in the P spin

configuration at positive bias. As one can see, transmission peaks take place shift with the applied

bias; however, there are always up-spin transmission peaks within the bias window, while all the

down-spin transmission peaks are out of the bias window. Therefore, the I_{P_up} is much larger than

I_{P_dw} according to the Landauer-Büttiker formula, and the SFE keeps nearly 100% in the whole

bias range. Fig. 4(c) and (d) correspond to the up- and down-spin transmission in the AP spin

configuration, respectively. Clearly, there is only down-spin transmission peak within the positive

bias window (> 0.2 V), while only up-spin transmission peak within the negative bias window (<

-0.2 V). Then only I_{AP_dw} can pass through the device at positive bias, while only I_{AP_up} can flow

through the device at negative bias. As a result, perfect bipolar spin-filtering and bipolar

spin-rectifying behaviors appear in the AP spin configuration. Since there is no any transmission

peaks at low bias for both up- and down-spin, a high GMR as high as 2.6×10^6% is obtained

within [-0.1, 0.1 V]. Also, from Fig. 4(a)-(d), one can see that the transmission peaks become

weaker and weaker with increasing bias. Once the overall reduction in transmission peak strength

outweighs any gains from the expanding bias window, the NDR behavior appears at 0.7 V in the

up-spin of P spin configuration and at $\mp$ 0.65 V in the up- and down-spin of AP spin

configuration.

The changes of transmission peaks can be understood by the spin-resolved band structures of

both the LE and RE at finite bias, the delocalization degree of the spin-polarized molecular

orbitals (MOs) within the bias window, and the symmetry of the Bloch wave functions of

corresponding subbands, which were plotted in Figs. 5-7, respectively. Fig. 5(a) and (b)

correspond to the case of P spin configuration at 0.7 and 1.15 V. From the middle panel of Fig.

5(a), one can see that for up-spin, there are three MOs (308-310) appearing in the bias window at

0.7 V. As shown in Fig. 6, the MO 310 is delocalized throughout the whole CSR, resulting in the

strong up-spin transmission peak around 0.2 eV. The MOs 308 and 309 locate within the energy

region where the up-spin π^*-subband of LE overlaps with the up-spin π-subband of RE. However,

as shown in Fig. 7, the isosurface plots of Γ-point Bloch wave functions indicate that the π (π-1)/

π^* (π^*+1)-subband has odd/even parity with regard to the mirror σ, which means the electron transmission between them is forbidden.[51,52] Therefore, there is no any transmission peak at the corresponding energy of MOs 308 and 309. For down-spin, there are five MOs (306-310) appearing in the bias window at 0.7 V. As shown in Fig. 6, the MO 306 is localized on the left part of CSR, while the MOs 307-310 locate within the energy region where the down-spin π^*-subband of LE overlaps with the down-spin π-subband of RE. As a result, there is no any down-spin transmission peak within the bias window. When the positive bias is further increased, the energy bands continue to shift downward and upward for the LE and RE, respectively. From the middle panel of Fig. 5(b), it can be found that there are six/seven MOs (306-311/305-311) within the bias window at 1.15 V for up- and down-spin, respectively. As shown in Fig. 6, the up-spin MO 311 distributes on the left and central part of CSR, leading to a very weak transmission around 0.3 eV, while the down-spin MO 305 is completely localized on the left part of CSR, resulting in this channel is strongly suppressed. All other MOs cannot contribute to the electron transmission due to the asymmetry of corresponding subbands in LE and RE. Fig. 5(c)-(f) correspond to the case of AP spin configuration at 0.65, 1.15, -0.65 and -1.15 V, respectively. The changes of transmission peaks at these four cases can also be explained similar to the cases of P spin configuration. For example, as shown in Fig. 5(f), when the negative bias is applied, the energy bands shift upward and downward for the LE and RE, respectively. There are six/five MOs (306-311/307-311) within the bias window at -1.15 V for up- and down-spin, respectively. As shown in Fig. 6, the up-spin MO 311 distributes on the left and central part of CSR, while the up-spin MOs 306 and 307 are completely localized on the right part of CSR. All other MOs have no contribution to the electron transmission due to the asymmetry of corresponding subbands in LE and RE. As a result, there is

only a very weak up-spin transmission around 0.25 eV.

4 Conclusions

In conclusion, we have investigated the spin transport properties of 4H-TAHDI-based multifunctional spintronic device with ZGNR electrodes by using the NEGF combined with the DFT. The results show that the systems can present perfect GMR, spin-filtering, bipolar spin-rectifying, and NDR effects simultaneously. These interesting phenomena were explained by the spin-resolved transmission spectrum, the spatial distribution of MOs within the bias window, the band structures of electrode, as well as the symmetry analyses of the corresponding subbands. These results might be helpful in the design of a high-performance multifunctional single-molecule spintronic device.

Acknowledgements

References

1 S. Sanvito, *Nat. Phys.*, 2010, **6**, 562-564.

2 M. N. Baibich, J. M. Broto, A. Fert, F. Nguyen Van Dau, F. Petroff, P. Etienne, G. Creuzet, A. Friederich and J. Chazelas, *Phys. Rev. Lett.*, 1988, **61**, 2472.

3 M. Gajek, M. Bibes, A. Barthélémy, K. Bouzehouane, S. Fusil, M. Varela, J. Fontcuberta and A. Fert, *Phys. Rev. B: Condens. Matter Mater. Phys.*, 2005, **72**, 020406(R).

4 M. Muller, M. Luysberg and C. M. Schneider, *Appl. Phys. Lett.*, 2011, **98**, 142503.

5 M. Lee, J. R. Williams, S. Zhang, D. Frisbie and D. Goldhaber-Gordon, *Phys. Rev. Lett.*, 2011, **107**, 256601.

6 P. Gütlich, H. A. Goodwin, *Top Curr. Chem.*, 2004, **233**, 1-47.

7 D. Antonangeli, J. Siebert, C. M. Aracne, D. L. Farber, A. Bosak, M. Hoesch, M. Krisch, F. J. Ryerson, G. Fiquet and J. Badro, *Science*, 2011, **331**, 64-67.

8 J. M. Kikkawa and D. D. Awschalom, *Nature*, 1999, **397**, 139-141.

9 K. Tsukagoshi, B. W. Alphenaar and H. Ago, *Nature*, 1999, **401**, 572-574.

10 S. Sanvito, *J. Mater. Chem.*, 2007, **17**, 4455-4459.

11 S. Schmaus, A. Bagrets, Y. Nahas, T. K. Yamada, A. Bork, M. Bowen, E. Beaurepaire, F. Evers and W. Wulfhekel, *Nat. Nanotechnol.*, 2011, **6**, 185-189.

12 X. Shen, L. L. Sun, Z. L. Yi, E. Benassi, R. X. Zhang, Z. Y. Shen, S. Sanvito and S. M. Hou, *Phys. Chem. Chem. Phys.* 2010, **12**, 10805-10811.

13 K. Xu, J. Huang, Z. Guan, Q. Li and J. Yang, *Chem. Phys. Lett.*, 2012, **535**, 111-115.

14 W. J. Cho, Y. Cho, S. K. Min, W. Y. Kim and K. S. Kim, *J. Am. Chem. Soc.*, 2011, **133**, 9364-9369.

15 J. Zeng and K. Q. Chen, *J. Mater. Chem. C*, 2013, **1**, 4014-4019.

16 J. Cai, P. Ruffieux, R. Jaafar, M. Bieri, T. Braun, S. Blankenburg, M. Muoth, A. P. Seitsonen, M. Saleh, X. Feng,

K. Müllen and R. Fasel, *Nature*, 2010, **466**, 470-473.

17 J. Guo, *Nanoscale*, 2012, **4**, 5538-5548.

18 K. S. Novoselov, A. K. Geim, S. V. Morozov, D. Jiang, Y. Zhang, S. V. Dubonos, I. V. Grigorieva and A. A. Firsov, *Science*, 2004, **306**, 666-669.

19 S. Y. Zhou, G. H. Gweon, A. V. Fedorov, P. N. First, W. A. de Heer, D. H. Lee, F. Guinea, A. H. C. Neto and A. Lanzara, *Nat. Mater.*, 2007, **6**, 770-775.

20 X. L. Li, X. R. Wang, L. Zhang, S. Lee and H. J. Dai, *Science*, 2008, **319**, 1229-1232.

21 F. Xia, V. Perebeinos, Y. M. Lin, Y. Wu and P. Avouris, *Nat. Nanotechnol.*, 2011, **6**, 179-184.

22 M. Fujita, K. Wakabayashi, K. Nakada and K. Kusakabe, *J. Phys. Soc. Jpn.*, 1996, **65**, 1920-1923.

23 X. Jia, J. Campos-Delgado, M. Terrones, V. Meuniere and M. S. Dresselhaus, *Nanoscale*, 2011, **3**, 86-95.

24 O. V. Yazyev and M. I. Katsnelson, *Phys. Rev. Lett.*, 2008, **100**, 047209.

25 Y. W. Son, M. L. Cohen and S. G. Louie, *Phys. Rev. Lett.*, 2006, **97**, 216803.

26 Y. W. Son, M. L. Cohen and S. G. Louie, *Nature*, 2006, **444**, 347-349.

27 W. Y. Kim and K. S. Kim, *Nat. Nanotechnol.*, 2008, **3**, 408-412.

28 M. Koleini, M. Paulsson and M. Brandbyge, *Phys. Rev. Lett.*, 2007, **98**, 197202.

29 K. Cai, Q. Yan and D. Zhao, *Chem. Sci.*, 2012, **3**, 3175-3182.

30 K. Cai, J. Xie and D. Zhao, *J. Am. Chem. Soc.*, 2014, **136**, 28-31.

31 K. Cai, J. Xie, X. Yang and D. Zhao, *Org. Lett.*, 2014, **16**, 1852-1855.

32 T. Ozaki, K. Nishio, H. Weng and H. Kino, *Phys. Rev. B: Condens. Matter Mater. Phys.*, 2010, **81**, 075411.

33 J. Taylor, H. Guo and J. Wang, *Phys. Rev. B: Condens. Matter Mater. Phys.*, 2001, **63**, 121104 (R).

34 J. Taylor, H. Guo and J. Wang, *Phys. Rev. B: Condens. Matter Mater. Phys.*, 2001, **63**, 245407(R).

35 M. Brandbyge, J. L. Mozos, P. Ordejón , J. Taylor and K. Stokbro, *Phys. Rev. B: Condens. Matter Mater. Phys.*,

2002, **65**, 165401.

36 J. M. Soler, E. Artacho, J. D. Gale, A. García, J. Junquera, P. Ordejón and D. Sánchez-Portal, *J. Phys.: Condens. Matter*, 2002 **14**, 2745-2779.

37 J. P. Perdew, K. Burke and M. Ernzerhof, *Phys. Rev. Lett.*, 1996, **77**, 3865-3868.

38 N. Troullier and J. Martins, *Phys. Rev. B: Condens. Matter Mater. Phys.,* 1991, **43**, 1993-2006.

39 Y. Ren and K. Q. Chen, *J. Appl. Phys*., 2010, **107**, 044514.

40 T. T. Wu, X. F. Wang, M. X. Zhai, H. Liu, L. P. Zhou and Y. J. Jiang, *Appl. Phys. Lett.*, 2012, **100**, 052112.

41 H. J. Monkhorst and J. D. Pack, *Phys. Rev. B: Condens. Matter Mater. Phys.*, 1976, **13**, 5188-5192.

42 M. Buttiker, Y. Imry, R. Landauer and S. Pinhas, *Phys. Rev. B: Condens. Matter Mater. Phys.*, 1985, **31**, 6207.

43 Y. H. Zhou, J. Zeng, L. M. Tang, K. Q. Chen and W. P. Hu, *Org. Electron.*, 2013, **14**, 2940-2947.

44 Q. H. Wu, P. Zhao, D. S. Liu and G. Chen, *Solid State Commun.*, 2013, **174**, 5-9.

45 H. Wan, B. Zhou, X. Chen, C. Q. Sun and G. Zhou, *J. Phys. Chem. C*, 2012, **116**, 2570-2574.

46 P. Zhao, D. S. Liu and G. Chen, *J. Chem. Phys.*, 2013, **139**, 084318.

47 Z. S. Su, M. K. Fung, C. S. Lee, W. L. Li and S. T. Lee, *Appl. Phys. Lett.*, 2008, **93**, 083301.

48 P. Dimitrakis, P. Normand, D. Tsoukalas, C. Pearson, J. H. Ahn, M. F. Mabrook, D. A. Zeze, M. C. Petty, K. T. Kamtekar, C. S. Wang, M. R. Bryce and M. Green, *J. Appl. Phys.,* 2008, **104**, 044510.

49 A. L. McWhorter and A. G. Foyt, *Appl. Phys. Lett.*, 1966, **9**, 300.

50 R. H. Mathews, J. P. Sage, T. C. L. G. Sollner, S. D. Calawa, C. L. Chen, L. J. Mahoney, P. A. Maki and K. M. Molvar, *Proc. IEEE*, 1999, **87**, 596-605.

51 Z. F. Wang, Q. X. Li, Q. W. Shi, X. P. Wang, J. L. Yang, J. G. Hou and J. Chen, *Appl. Phys. Lett.*, 2008, **92**, 133114.

52 Z. Li, H. Qian, J. Wu, B. Gu and W. Duan, *Phys. Rev. Lett.*, 2008, **100**, 206802.

Figure Captions

Fig. 1 (a) Schematic view of the 4H-TAHDI-based multifunctional spintronic device. The labels LE, CSR, and RE represent the left electrode, the central scattering region, and the right electrode, respectively. The ZGNR electrodes have been marked in cyan for clarity. The gray, blue, red and white spheres indicate the carbon, nitrogen, oxygen, hydrogen atoms, respectively. (b) Spin density for P and AP spin configurations under zero bias. The red and cyan colors stand for the up- and down-spin components, respectively.

Fig. 2 (a) Calculated total I-V curves for P and AP spin configurations. (b) and (c) Spin-resolved I-V curves for two spin configurations, respectively.

Fig. 3 (a)-(c) Calculated magnetoresistance ratio (MR), spin-filtering efficiency (SFE), and rectification ratio (RR) as a function of the applied bias.

Fig. 4 Spin-resolved transmission as a function of both electron energy and bias for two spin configurations. (a) and (b) correspond to the up- and down-spin transmission in the P spin configuration at positive bias. (c) and (d) correspond to the up- and down-spin transmission in the AP spin configuration, respectively. The two dotted blue lines denote the electrochemical potentials of left and right electrodes. The Fermi level E_F has been set at zero and the zero-bias transmission spectrum has been marked in red for clarity.

Fig. 5 Spin-resolved band structure for the left (left panels), right electrode (right panels), and

transmission spectrum (middle panels). The solid black and dashed red lines indicate the up- and down-spins, respectively. (a) and (b) correspond to the case of P spin configuration at 0.7 and 1.15 V. 5(c)-(f) correspond to the case of AP spin configuration at 0.65, 1.15, -0.65 and -1.15 V, respectively. The two horizontal dashed blue lines denote the electrochemical potentials of left and right electrodes, and the Fermi level E_F has been set at zero. The positions of molecular orbitals within the bias window are shown with short black bars for up-spin and short red bars for down-spin.

Fig. 6 Spatial distribution of the spin-polarized molecular orbital (MO) within the bias window for two spin configurations. Those, having no contribution to the electron transmission due to the asymmetry of corresponding subbands in left and right electrodes, are not shown here. The isosurface level is taken as 0.05 ($Å^{-3}·eV^{-1}$).

Fig. 7 Isosurface plots of Γ-point Bloch wave functions of the π (π-1)/ π^* (π^*+1)-subbands, which has odd/even parity with regard to the mirror σ, respectively. The isosurface level corresponds to 0.05 ($Å^{-3}·eV^{-1}$).

(a)   ● C   ● N   ● O   ○ H
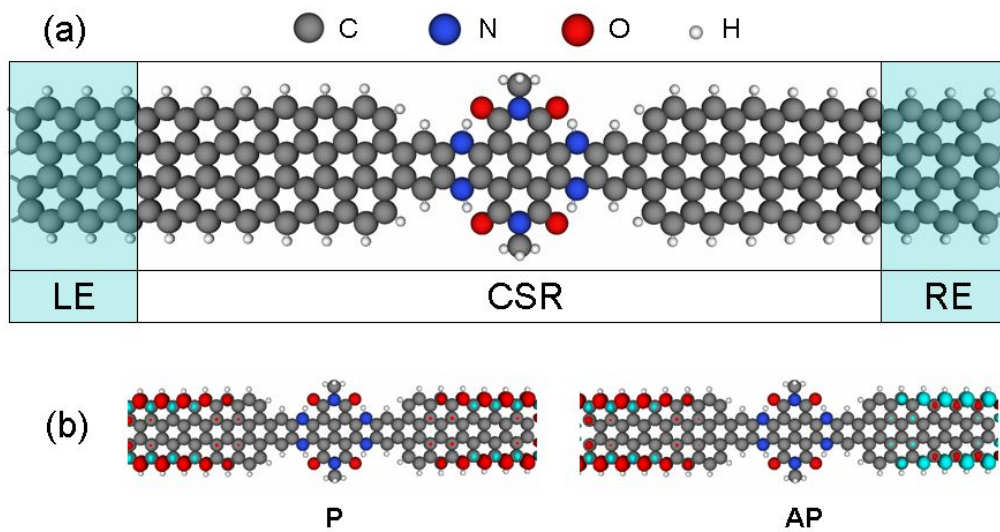
LE   CSR   RE

(b)

P   AP

Fig. 1

Fig. 2

Fig. 3

Fig. 4

Fig. 5

P_0.7 V_up_310 P_0.7V_dw_306 P_1.15V_up_311 P_1.15V_dw_305

AP_0.65V_dw_310 AP_0.65V_dw_309 AP_0.65V_dw_308 AP_0.65V_dw_307

AP_0.65V_dw_306 AP_1.15V_dw_311 AP_1.15V_dw_305 AP_-0.65V_up_310

AP_-0.65V_up_309 AP_-0.65V_up_308 AP_-0.65V_up_307 AP_-0.65V_up_306

AP_-1.15V_up_311 AP_-1.15V_up_307 AP_-1.15V_up_306

Fig. 6

Fig. 7

TOC
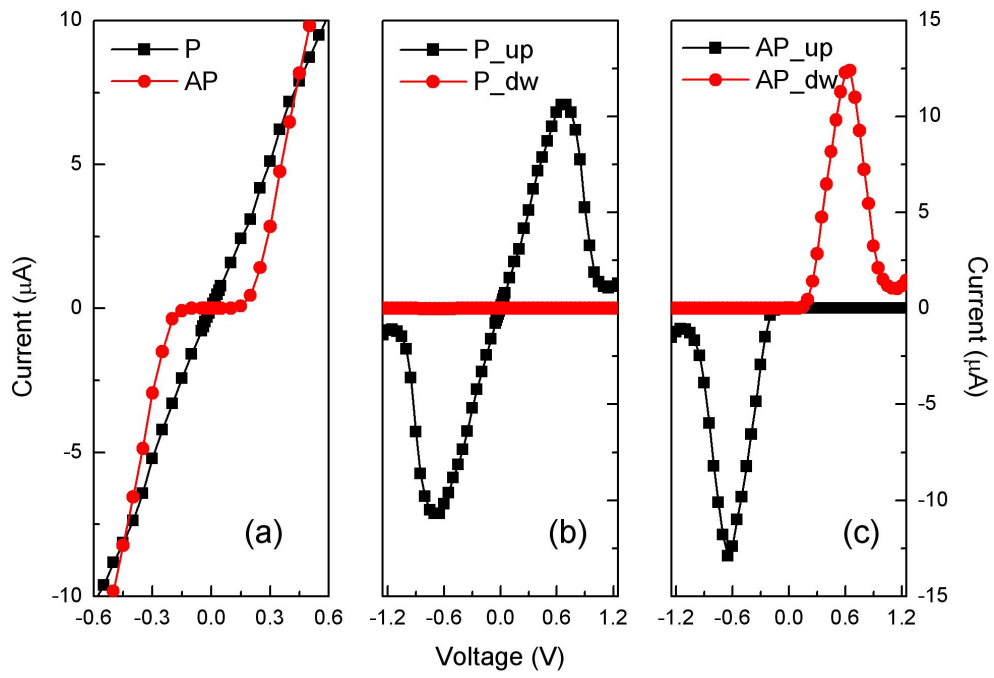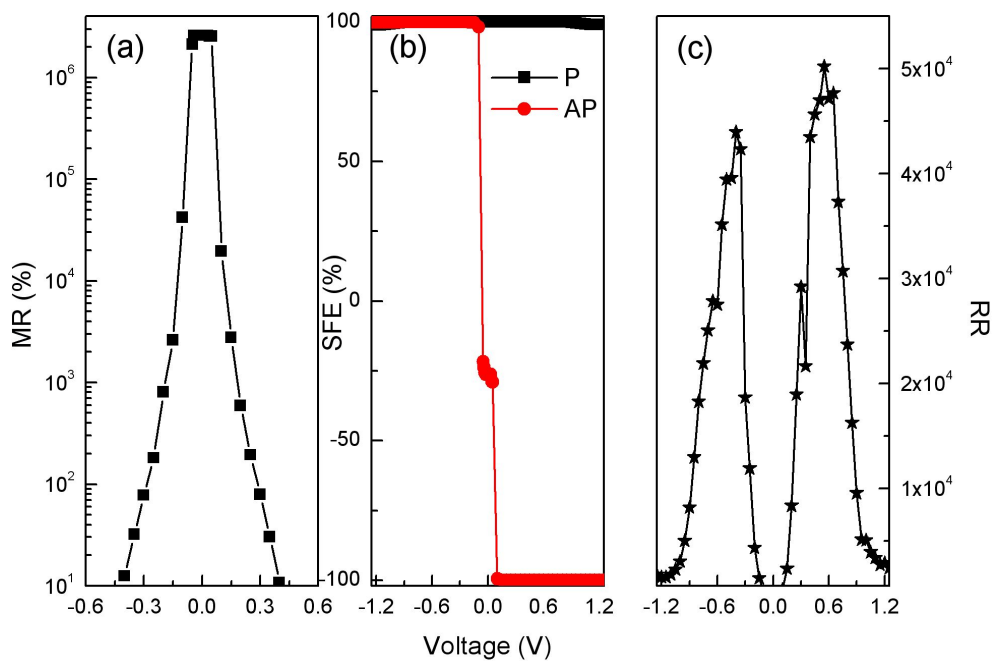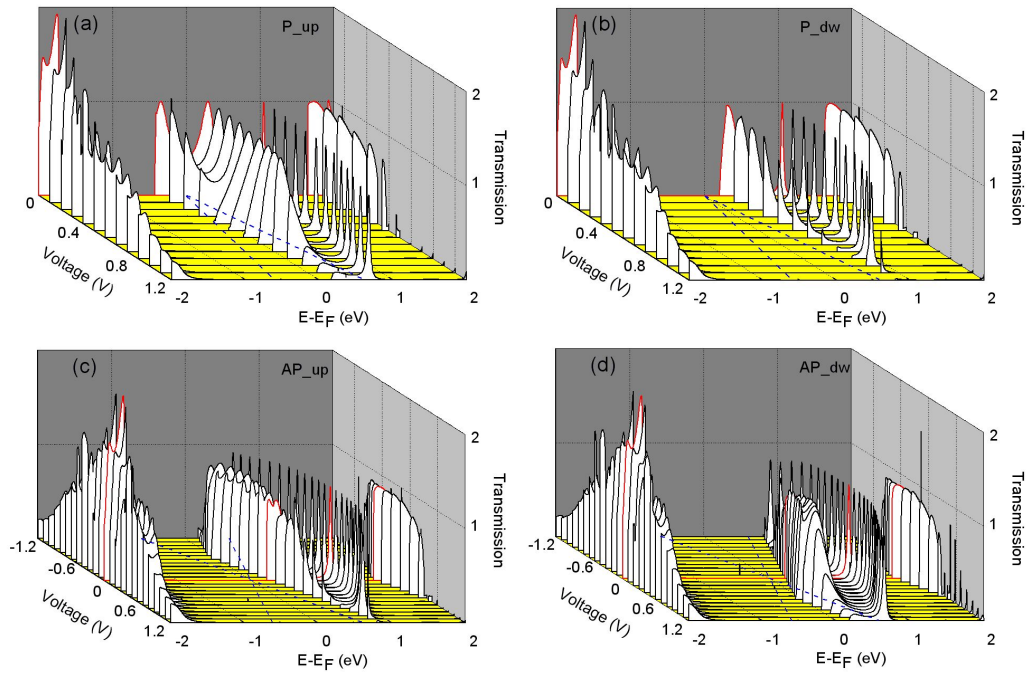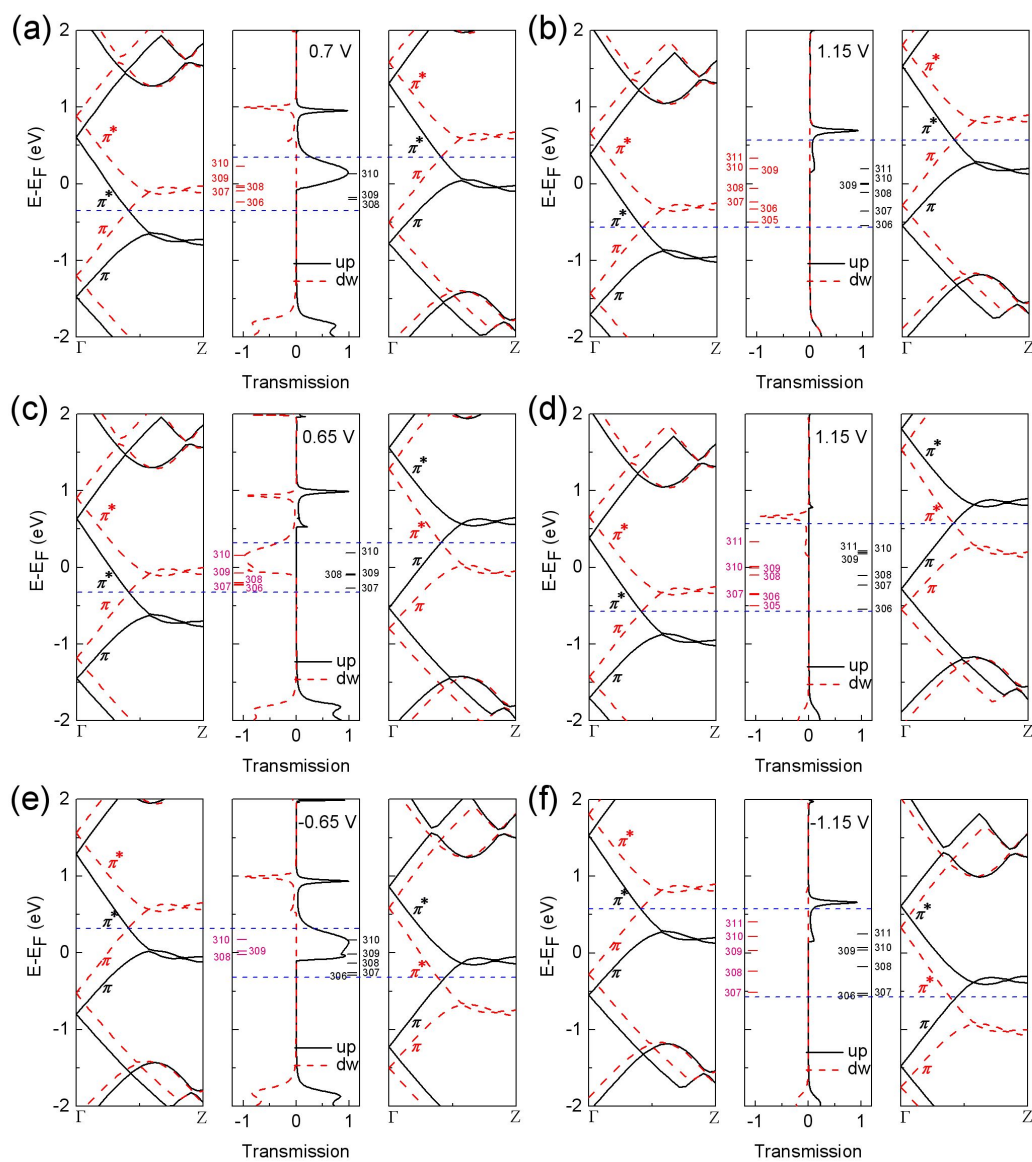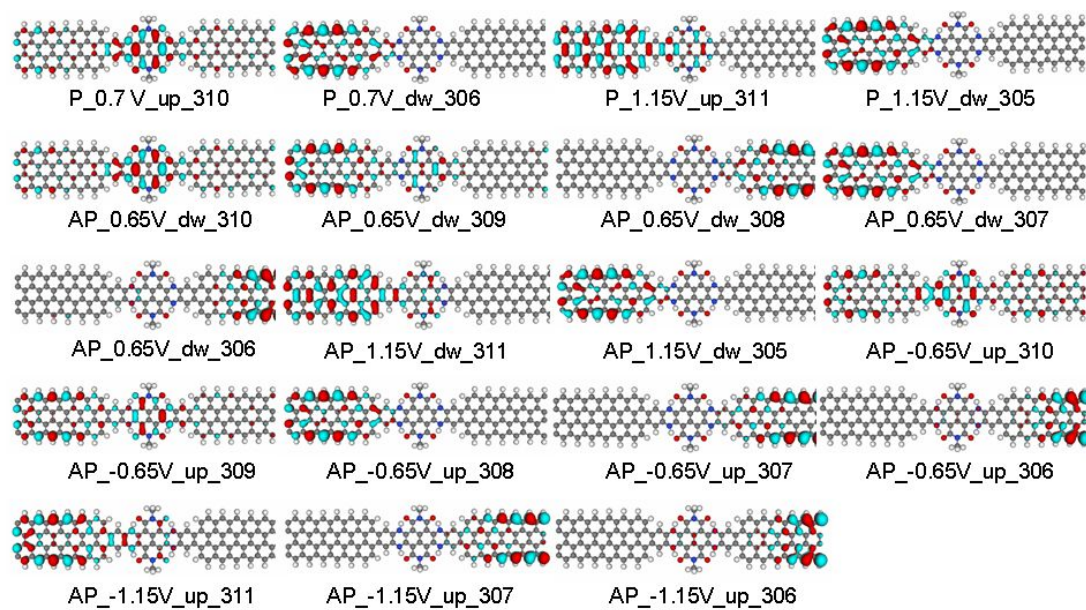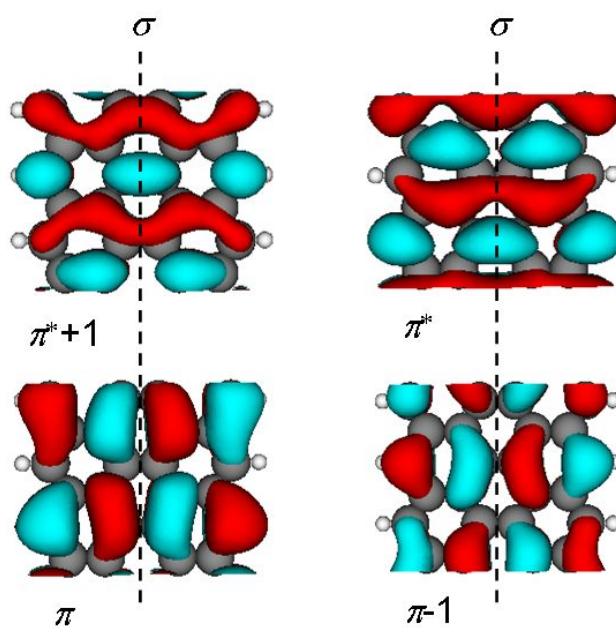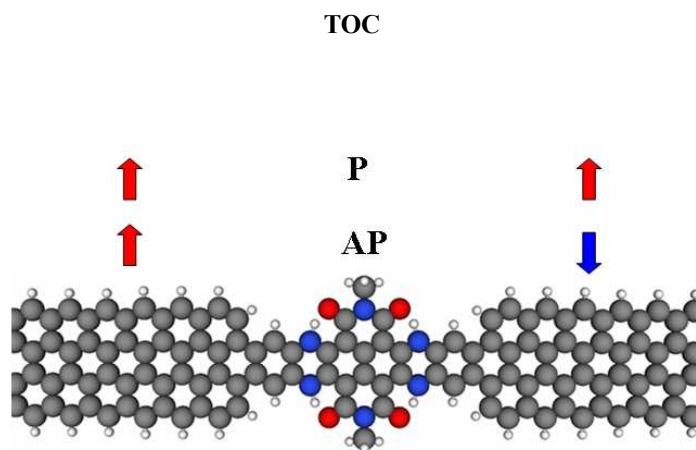

The 4H-TAHDI-based spintronic device can exhibit perfect giant magnetoresistance, spin-filtering, bipolar spin-rectifying, and negative differential resistance effects simultaneously.